Geophysical Journal International

Ambient noise tomography of the Pyrenees and the surrounding regions: inversion for a 3-D *Vs* model in the presence of a very heterogeneous crust

Marie Macquet,[1,2] Anne Paul,[1,2] Helle A. Pedersen,[1,2] Antonio Villaseñor,[3]
Sébastien Chevrot,[4] Matthieu Sylvander,[4] David Wolyniec[1,2] and Pyrope Working Group*

[1]*Université Grenoble Alpes, ISTerre, F-38041 Grenoble, France. E-mail: marie.macquet@ujf-grenoble.fr*
[2]*CNRS, ISTerre, F-38041 Grenoble, France*
[3]*Institute of Earth Sciences Jaume Almera, ICTJA-CSIC, Barcelona, Spain*
[4]*Université Paul Sabatier, CNRS, IRAP, Observatoire Midi Pyrénées, Toulouse, France*

SUMMARY

The lithospheric architecture of the Pyrenees is still uncertain and highly debated. Here, we provide new constraints from a high-resolution 3-D *S*-wave velocity model of the Pyrenees and the adjacent foreland basins. This model is obtained from ambient noise tomography on records of temporary and permanent seismic arrays installed in southwestern France and northern Spain. We first computed group velocity maps for Rayleigh waves in the 5 to 55 s period range using noise correlation stacks at 1500–8500 station pairs. As the crust is very heterogeneous, poor results were obtained using a single starting model in a linearized inversion of group velocity dispersion curves for the shear wave structure. We therefore built a starting model for each grid node by full exploration of the model space. The resulting 3-D shear wave velocity model is compared to data from previous geophysical studies as a validation test. Despite the poor sensitivity of surface waves to seismic discontinuities, the geometry of the top of the basement and the Moho depth are retrieved well, except along the Cantabrian coast. Major reflectors of the ECORS deep seismic sounding profiles in the central and western Pyrenees coincide with sharp velocity gradients in our velocity model. We retrieve the difference between the thicker Iberian crust and the thinner European crust, the presence of low-velocity material of the Iberian crust underthrust beneath the European crust in the central Pyrenees, and the structural dissymmetry between the South Pyrenean Zone and the North Pyrenean Zone at the shallow crustal level. In the Labourd–Mauléon–Arzacq region (western Pyrenees), there is a high *S*-wave velocity anomaly at 20–30 km in depth, which might explain the positive Bouguer anomaly of the Labourd Massif. This high-velocity lower crust, which is also detected beneath the Parentis area, might be an imprint of the Albian–Aptian rifting phase. The southeastern part of the Massif Central has an unusual velocity structure, with a very shallow Moho (21–25 km) above an uppermost mantle with anomalously low shear wave velocity.

Key words: Surface waves and free oscillations; Seismic tomography; Crustal structure; Europe.

1 INTRODUCTION

The Pyrenean range and the adjacent foreland basins resulted from the continent–continent collision between the Iberian and Eurasian plates. A sequence of Mesozoic extension phases, related to the opening of the northern Atlantic Ocean and the Bay of Biscay, was accompanied by a $\sim$35° counter-clockwise rotation of Iberia. This rotation created a first compression phase in the Pyrenees.

Convergence between Africa and Europe subsequently resulted in a second compression phase starting in the early Cenozoic (see e.g. Choukroune 1992). As the motion of Iberia with respect to a stable Europe remains uncertain, the relative contributions of convergence and shear accommodated in the Pyrenees, as well as their timing, have been debated since the emergence of the concept of plate tectonics in the 1960s (Le Pichon *et al.* 1970; Choukroune & Mattauer 1978; Sibuet *et al.* 2004; Vissers & Meijer 2012, and references therein).

As the lithosphere retains the memory of this complex history of plate convergence, rifting and transcurrent motion, investigations into the Pyrenean architecture by geophysical means in combination with geological studies are key to the reconstruction of the evolution of the Pyrenees.

A major step forward was provided by the ECORS deep seismic sounding profile in the central Pyrenees (ECORS Pyrenees Team 1988; Choukroune *et al.* 1989; Roure *et al.* 1989), which was followed by the western Pyrenees–Arzacq profile (Daignières *et al.* 1994). The 250-km-long central Pyrenees profile was the first controlled-source survey across an entire orogenic belt. This showed a fan shape structure with major reflectors of opposite dips in the northern and southern parts of the range, an abrupt 15 km change in crustal thickness beneath the axial part, and deep northward-dipping reflectors in the European mantle, which were interpreted as traces of the subducted Iberian crust (Choukroune *et al.* 1989). A sharp Moho step of about 15 km between the thick Iberian crust and the thinner European crust was also observed on the western Pyrenees–Arzacq profile (Daignières *et al.* 1994).

Previous passive seismological studies have been limited to the axial part of the range, because of the limited station coverage. Souriau & Granet (1995) proposed the first *P*- and *S*-wave traveltime tomography of the Pyrenees down to 200 km in depth, using local and teleseismic earthquakes. They found a very heterogeneous upper crust with sharp and strong velocity contrasts, above a more homogeneous lower crust. Their tomography, however, suffered from the poor and non-uniform station coverage, as well as from the limited north–south aperture of the array. Souriau & Granet (1995), Souriau *et al.* (2008) and Chevrot *et al.* (2014) inverted the teleseismic traveltimes recorded by continuously improving the seismic arrays to image the upper mantle beneath the Pyrenees. Chevrot *et al.* (2014), however, showed that the results of Souriau & Granet (1995) and Souriau *et al.* (2008) had to be reconsidered, due to lacking or inappropriate crustal corrections. Chevrot *et al.* (2014) concluded that the lithospheric structure of the Pyrenees is controlled by inherited NE–SW-trending Variscan faults, without any trace of the subducted oceanic lithosphere. Their tomography confirms the recent geological models of Lagabrielle & Bodinier (2008) and Jammes *et al.* (2009), which proposed that the Pyrenean convergence was preceded by a rifting phase with extreme crustal thinning and mantle denudation. This rifting phase of the Albian–Aptian age was followed by the late Cretaceous convergence, which explains the presence of rock of upper-mantle origin at the surface (lherzolites of the northern Pyrenean zone; Lagabrielle *et al.* 2010), or at deeper levels in the crust (high-density bodies that induce the Bouguer anomaly of the Labourd Massif; Jammes *et al.* 2010). However, the presence of these high-density high-velocity bodies in the crust of the North Pyrenean Zone has never been confirmed by seismic tomography, due to the lack of a high-resolution 3-D crustal model of the Pyrenees and their surroundings.

The obtaining of a 3-D crustal velocity model of the Pyrenees was one of the main objectives of the Pyrenees Observational Portable Experiment (PYROPE) project (Chevrot *et al.* 2014), which was
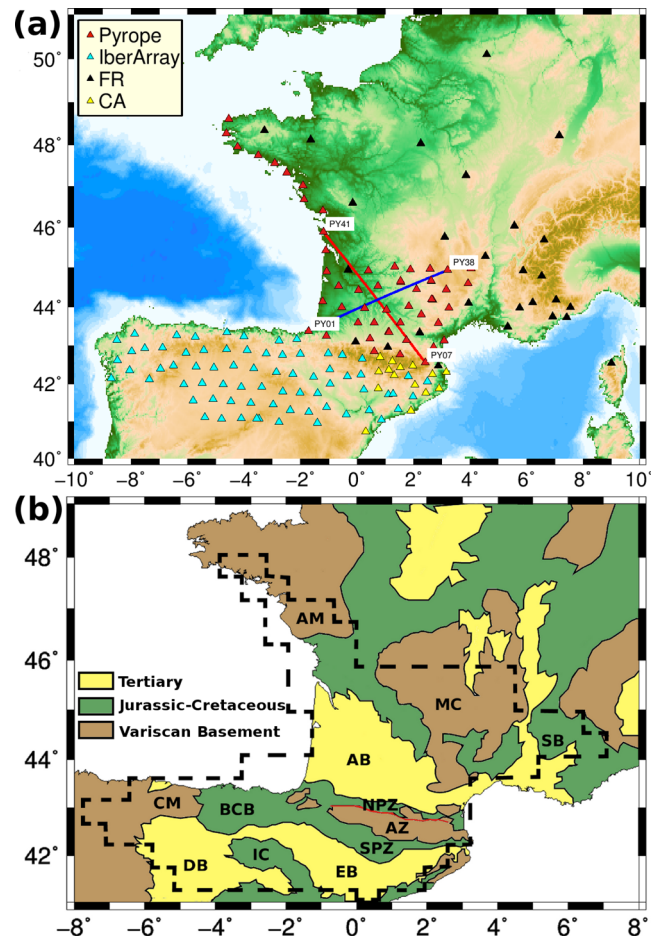
Figure 1. (a) Map of the 158 seismic broadband stations used in the present study, corresponding to 12 324 station pairs. Red and blue lines, stations pairs used in Fig. 2. (b) Simplified geological map of the study zone. Red line, the North Pyrenean fault; dashed black line, limits of the well-resolved zone of the tomography; AB, Aquitaine basin; AM, Armorican Massif; AZ, Axial Zone of the Pyrenees; BCB, Basque–Cantabrian basin; CM, Cantabrian mountains; DB, Duero basin; EB, Ebro basin; IC, Iberian chain; MC, Massif Central; NPZ, North Pyrenean Zone; SB, southeastern basin; SPZ, South Pyrenean Zone.

associated with the northern footprint of the IBERARRAY project (Díaz *et al.* 2009). These projects relied on temporary seismic arrays, and together with the permanent stations, these provided dense and uniform coverage of a broad area (Fig. 1a). Fig. 1(b) shows that the seismic array encompasses the Pyrenees mountain belt, the southern part of the French Massif Central, part of the Armorican Massif in France, part of the Cantabrian Mountains, part of the Iberian Chain in Spain, the large Aquitaine and southeast sedimentary basins in France, and the Ebro and Duero basins in Spain.

This study was aimed at computing a 3-D crustal model of the study region using ambient noise tomography. Ambient noise tomography relies on experimental validation and theoretical validation that the Green's function between two receivers emerges from the time correlation of a random field recorded by the two receivers (Campillo & Paul 2003; Shapiro & Campillo 2004). As the Green's function is dominated by the fundamental mode of the surface waves for stations located at the surface, group or phase velocity maps can be constructed by correlating the long-duration noise records at the station couples of a seismic array (Shapiro *et al.* 2005).

Since these initial reports, ambient noise tomography has been widely applied at regional and continental scales. In contrast to 'traditional' crustal tomography using local and regional earthquakes, ambient noise tomography is a method that can be used in the absence of seismicity. This is an important advantage for the study region, where the seismicity is moderate and is concentrated in the Pyrenees. Another advantage of ambient noise tomography is that the signal is strong in the microseismic frequency band (7 and 14 s), which is useful for surface wave imaging of the crust, whereas surface wave signals from earthquakes are generally strongly scattered and are complex to analyse at periods lower than 15–20 s. The usefulness of group or phase velocity maps for crustal structure investigation is limited, however, as they lack information on velocity variations with depth. As this study region has a very heterogeneous upper-crustal structure with thick sedimentary basins and crystalline massifs, one particular aim of this study is to develop a robust depth inversion to obtain a detailed 3-D shear wave velocity (*Vs*) model of the study area. This is based on a combination of full exploration of the model space followed by linear inversion.

This report is organized as follows. We first go into some detail on the data processing, as ambient noise tomography is very efficient and robust if the processing is adapted to the data set. We then explain the computation of the dispersion curves and the inversion for group velocity maps, and the technique developed to invert group velocities for a 3-D *S*-wave velocity model. Finally, the 3-D model is discussed and compared to other geophysical and geological data. This first 3-D crustal *Vs* model will not only bring key geophysical constraints to geodynamic models of the Pyrenees, but it might also help in the understanding of the anomalous patterns of seismic-wave propagation across the range (Chazalon *et al.* 1993; Sens-Schönfelder *et al.* 2009), and hence contribute to seismic-hazard assessment.

2 DATA PROCESSING

2.1 Data and pre-processing

The tomography is based on a composite data set from four broadband seismic arrays (see Fig. 1a), as 25 permanent stations in France, 14 permanent stations in northern Spain, and two large temporary arrays. The PYROPE temporary array in southwestern France was composed of 49 stations, while the northern section of the IBER-ARRAY project in Spain is composed of 70 stations. This data set, for which we used data between 2011 February and 2011 December, covers all of southwestern France and northern Spain, with an interstation distance of approximately 60 km. The total of 158 stations corresponds to 12 403 interstation pairs that were dominated by path lengths of 100–500 km, with a minimum path length of 40 km, and a maximum of 1240 km. We subsequently calculated the correlations for all of these paths, as described below.

Prior to the correlations, we applied standard pre-processing to the continuous data, which was organized as daily files. This included mean and trend removal, low-pass filtering (zero-phase filter) at 1.6 Hz, decimation to a 4 Hz sampling rate and deconvolution of the instrument responses. As the instrument response influences the correlations, especially for long periods where the phase responses differ the most, special care was taken in this last step, with verification of the metadata from field sheets and *a posteriori* checks of the phase coherency across the array for the earthquake data.

2.2 Choice of correlation processing

When calculating noise correlations, it is necessary to overcome some difficulties. Contrary to earthquake-based tomography, one of the essential steps in the calculation of noise correlations is to remove punctual events, and in particular, earthquakes. Indeed, seismic waves from these events are at least partly coherent across the array in the period interval that we used, and can introduce systematic bias into the correlations. The spectral content of the noise was dominated by the two microseismic peaks (at periods of 7 s and 14–15 s), and the achieving of high signal-to-noise ratios (SNRs) at long periods for the path lengths considered here can be a challenge in noise correlation. Finally, the period of the study must be sufficiently long, typically a year, to avoid dominance by a single noise source (e.g. Pedersen *et al.* 2007; Froment *et al.* 2010). In the case of Europe, the noise sources in the winter are localized in the northern Atlantic (Stehly *et al.* 2006; Kedar *et al.* 2007; Hillers *et al.* 2012), and in the Mediterranean Sea for the secondary microseism peak (Chevrot *et al.* 2007), and including the summer months is sufficient to obtain stable correlations (see e.g. fig. 2 of Poli *et al.* 2013). A specific problem in this study was the presence of numerous aftershocks of the Tohoku-Oki earthquake of 2011 March.

Different processing strategies have been used to overcome these general difficulties in noise correlation. In initial studies, the amplitudes were fully suppressed by reducing the data to their sign; that is, so-called 1-bit processing (e.g. Campillo & Paul 2003; Shapiro & Campillo 2004; Stehly *et al.* 2006; Cupillard *et al.* 2011). While it strongly reduces the influence of earthquakes, this processing acts like a severe bandpass filter around the dominant frequencies. The other end-member approach is based on linear correlation, using short (e.g. 1 or 4 h) time windows, out of which those with highest energy are rejected, possibly using some pre-whitening prior to the correlation (Groos *et al.* 2012; Poli *et al.* 2012a; Seats *et al.* 2012). Intermediate approaches have also been successful, such as using the phase of the signal, rather than fully reducing the signal to its sign (Baig *et al.* 2009; Schimmel *et al.* 2011), or applying various types of time normalization (Bensen *et al.* 2007). As demonstrated by Stehly & Cupillard (2014), the processing partly determines which part of the noise field contributes to the correlation. Therefore, at the present stage, there is no universal recipe for noise correlation, as the processing will depend on the noise field, which is influenced in particular by the geographical location of the array. Also, the scope of the noise processing will imply different choices; for example, linear correlation over short time windows (Poli *et al.* 2012a,b; Boué *et al.* 2013) appears to be particularly well adapted to expect body waves from the deep crust, and at a global scale.

In our case, the problem with the many aftershocks from the Tohoku-Oki earthquake led us to exclude the linear processing in short time windows. Indeed, our tests showed that a very large number of windows had to be rejected to obtain non-biased surface waves, although the final SNR was consequently lower than when we applied 1-bit processing.

Fig. 2 illustrates that the choice of the precise processing depends not only on the array location, but also on the station-pair alignment as compared to the azimuths of the dominating noise sources. Fig. 2 shows a comparison of the SNRs for two different versions of 1-bit correlation.

1. *Method 1:* the signals are reduced to 1-bit, and the signals are then whitened. The consequence of using this processing is to carry out the correlations in different frequency intervals, as the 1-bit signal reduction tends to narrow the useable frequency interval.
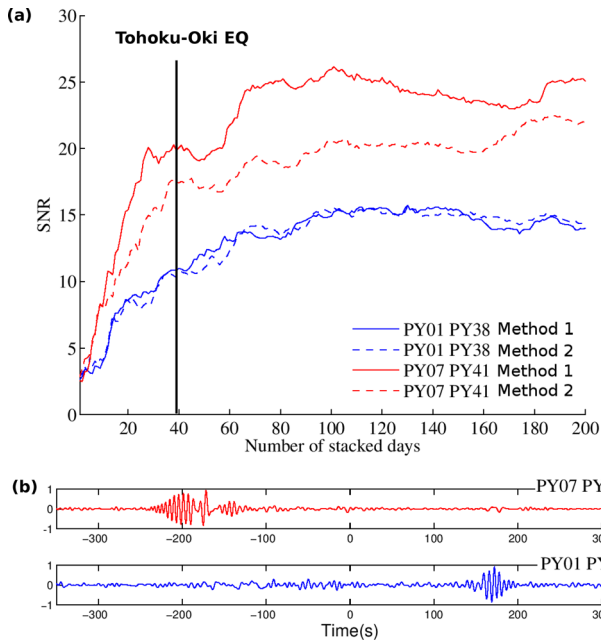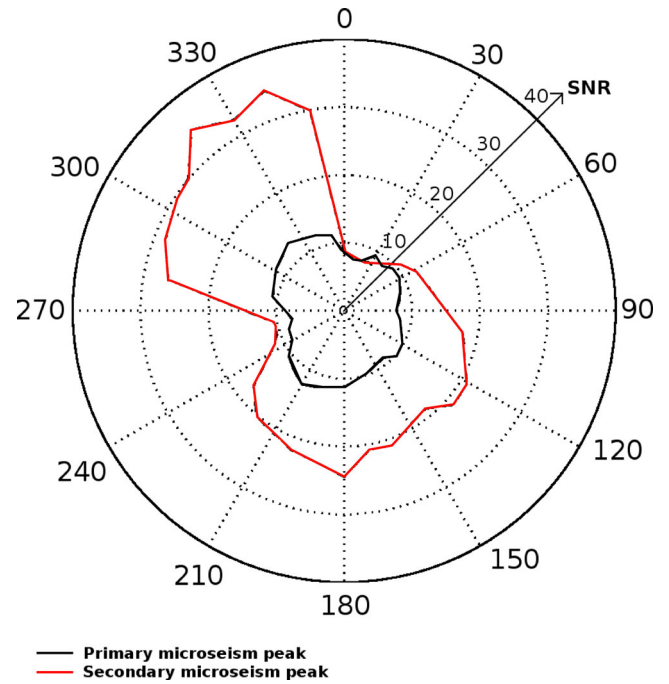
Figure 2. (a) Evolution of the signal-to-noise ratio (SNR) for two stations pairs (Fig. 1a, blue and red) as a function of the number of days stacked, for the different types of processing. Dashed line, spectral whitening then 1-bit; solid line, 1-bit then spectral whitening; black solid line, date of the M9.1 Tohoku-Oki earthquake. (b) Resulting cross-correlations (200 d stacked) for the two paths used in (a) for the 1-bit then spectral whitening processing.

The whitening is therefore efficient only in this reduced frequency interval; however, the SNR within that frequency interval is high.

2. *Method 2:* the whitening is applied before the 1-bit signal reduction. This yields a more broadband signal, but potentially with a lower SNR within that frequency band. As the bandpass is wider, the number of correlations that need to be carried out might be lower, thereby decreasing the required computational time.

Fig. 2 shows the result for one of the station pairs (PY07/PY41) for which Method 1 (solid line) yields a higher SNR and a faster convergence than Method 2 (dashed line). This station pair is oriented NW–SE (Fig. 1a); that is, in the direction of maximum amplitude of the incoming noise (Fig. 3). For the other station pair (PY01/PY38), which is perpendicular to the dominant noise direction, the two methods give very similar results. Note that the SNR (calculated as the ratio of the maximum amplitude of the Rayleigh wave to the rms amplitude of the noise in a 500 s long-time window starting 150 s after the Rayleigh wave train) stabilizes over approximately 2 months. This might depend on the date of the beginning of the data set, as the first two months cover a period where the noise field changes from winter to summer conditions. The management of the Tohoku-Oki aftershocks appears satisfactory, as no significant changes in the SNR are detected, even though a slight decrease is observed for one of the station pairs immediately after the event (Fig. 2, PY07/PY41). Using the SNR and the number of kept paths (9758 correlations for method 1, 7405 for method 2, using a SNR threshold of 5 and the whole frequency band), we settled on a processing suite that included amplitude clipping (1-bit) and whitening prior to correlation.

The use of the WHISPER software package (Briand *et al.* 2013) strongly reduced the calculation time of the correlations. It was thus easily feasible to apply Method 1, where prior to 1-bit reduction, whitening and correlation, the data were pre-filtered in three differ-

Figure 3. Azimuthal distribution of the signal-to-noise ratio (SNR) for the 1-bit then spectral whitening processing. Solid black line, primary microseism peak (14–15 s); solid red line, secondary microseism peak (7 s).

ent period bands: 5–30 s, 20–40 s and 30–55 s. Correlations are 1-d computed and stacked over the 11-months period.

2.3 Directivity of the seismic noise field in the study area

Fig. 3 shows the directivity of the noise field on our seismic array during the 2011 February to 2011 December period, for the first and second microseismic peaks. The SNR was computed for all of the paths, and averaged in 10° band azimuths. The secondary microseism (Fig. 3, red line) shows higher energy than the primary microseisms (Fig. 3, black line). We can clearly see a major source located in the direction N320°. Here, only the orientation, and not the exact location, can be determined, but this might have been associated with the Greenland source (Stehly *et al.* 2006; Hillers *et al.* 2012). Two more minor sources can be identified in directions N190°–N120° (probably in the southern Atlantic Ocean), and N110°–N140° (possibly in the Mediterranean Sea).

3 GROUP VELOCITY TOMOGRAPHY

3.1 Dispersion curves

Some studies have used the symmetry of the correlations as a quality criterion (Stehly *et al.* 2009); however, the symmetry properties of our correlations are strongly frequency dependent (see previous section). Therefore, we stacked the correlations for positive and negative times to enhance the part of the signal that is symmetric, as this procedure (slightly) increases the SNR. We only calculate the group velocities when the SNR of the stacked non-filtered trace is higher than five, with further criteria subsequently applied to the group velocity dispersion quality, as indicated below. A SNR of five is not sufficient to avoid unwarranted oscillations in the phase velocities, which is why we used the more stable group velocities for the tomography. Table 1 shows the number of paths kept after

Table 1. Number of paths kept at each step of the data selection before the final inversion for the group velocity (see text for further explanations). SNR, signal-to-noise ratio; rms, root mean square.

Total						12 403					
Period range (s)		[5–30]				[20–40]				[30–55]	
SNR > 5		9758				8164				5625	
Period (s)	5	10	15	20	25	30	35	40	45	50	55
$d > 3\lambda$ and no jump	9536	9136	8536	7848	7131	6399	3872	2332	1993	1700	1451
Without unrealistic paths	8436	8218	8167	7429	6730	6004	3682	2192	1933	1655	1415
Variance reduction (%)	78	65	64	67	60	46	46	50	43	41	37
Final rms (km s^{-1})	0.045	0.024	0.015	0.007	0.004	0.015	0.015	0.023	0.019	0.016	0.014

this selection. As shown by the azimuthal averages (Fig. 3), the majority of the correlations have a SNR of ≥10.

We used multiple filter analysis (Levshin *et al.* 1989) to calculate the group velocity dispersion of the Rayleigh wave for the 5–55 s period. We applied the calculations independently for each of the three frequency bands (5–30 s, 20–40 s, 30–55 s) and applied a linear weighted average of the retrieved curves in the frequency interval that overlapped, to obtain a unique dispersion curve for each station pair.

For the subsequent inversion for the group velocity maps at each period, we used only paths for which the interstation distance was longer than three wavelengths. The number of paths varied between 1500 at 55 s and 9500 at 5 s (out of 12 403 station pairs; see Table 1). For each of these curves, we finally evaluated the continuity of the dispersion curves and excluded the (narrow) frequency intervals where the group velocity curve had significant discontinuities (jumps >0.1 km s^{-1}). The final data rejection was carried out based on an initial run of the inversion (see next section). Fig. S1 shows three examples of the dispersion curves used for the group velocity tomography. The blue curve is in the Pyrenees range, the red one in the Aquitaine basin, and the green one in the Bay of Biscay. We can see some differences that characterize each region. At low period, the group velocities are higher for the curve corresponding to the Pyrenees, as we do not expect sedimentary cover in this region, contrary to the other regions. At higher periods, the dispersion curves for the Aquitaine Basin and the Bay of Biscay group the velocities, as the crust is thinner in these areas. As the Moho is the most superficial in the Bay of Biscay, the dispersion curve that corresponds to this region is stabilized at 25 s, whereas the group velocities continue to increase in the other regions.

3.2 Group velocity tomography

3.2.1 Method

For each frequency, the remaining group velocities between station pairs were used to obtain a group velocity map, using the method of Barmin *et al.* (2001). We here present a brief summary of the method and refer the reader to Mordret *et al.* (2013) for detailed discussion. To estimate the model *m*, we minimize the penalty function, such that:

$$S(m) = (Gm - d)^T C_d^{-1}(Gm - d) + m^T Qm, \qquad (1)$$

where *d* is the data vector, *G* is the forward operator, C_d is the data covariance and *Q* is the regularization matrix. The first term of the penalty function is the data misfit, and the second term contains the regularization parameters. For the inversion, we used a regular grid of 40 km × 40 km, as our resolution analysis showed the necessity for lateral smoothing of the model of approximately 50 km at a 5 s

period (see below). Decreasing the cell size increases the CPU time without increasing the resolution.

To calculate the regularization parameters, we used the L-curves. The Barmin *et al.* (2001) method uses four smoothing parameters. Only two of them, lateral smoothing and damping, have a significant influence on the inversion, while the remaining two, related to path density which is everywhere high in our case, do not influence the inversion. The interdependence between the two remaining L-curves was addressed by prior knowledge on parameter variations for different periods. Indeed, the lateral variations of the group velocities were significantly higher at short periods than at long periods, due to the lateral heterogeneity of the area in the upper crust, and in particular due to the presence of sedimentary basins in some areas. Based on forward modelling of dispersion curves in areas with and without thick sedimentary basins and on the shape of the L-curve (shown in Fig. S2), we imposed damping that corresponds to maximum variations of group velocities of ±20 per cent at short periods and ±8 per cent at long periods. The inferred lateral smoothing was therefore also frequency dependent, and increased linearly from 50 km at a 5 s period, to 100 km at a 30 s period, and then remained constant beyond this period. This smoothing is consistent with the wavelength of surface waves, which varied between approximately 15 km at a 5 s period and 220 km at a 55 s period, and the interstation distance, which was about 60 km.

We finally used the inversion to carry out a final data quality check, following Stehly *et al.* (2009). At each frequency (1 s period intervals between 5 and 55 s) we first inverted the data with all of the paths. In a second inversion, we rejected the paths where the differences between the predicted and observed traveltimes were >2-fold the average of all of the traveltime differences. At long periods, the number of rejected paths was insignificant, while up to 1000 paths were rejected at short periods. Table 1 shows the number of paths kept after this selection, while Fig. S3 shows the path densities for the 5, 30 and 55 s periods. Even at 55 s, the number of paths in each cell is typically >40. This procedure, for which manual visual inspection was carried out for a subset of paths, was aimed at rejecting unrealistic paths. We carried out the inversion on this final data set, with a homogeneous starting model built as the average of the group velocities observed.

3.3.2 Group velocity maps

Fig. S4 shows an example of the inversion result at a 15 s period, where an interpolated map is also shown (linear 2-D interpolation between the centres of adjacent cells). For the best visualization of the results and the comparison with the geology of the area, we use such interpolated maps.

Fig. 4 shows the group velocity maps at 5, 10, 20, 30, 40 and 50 s periods; that is, corresponding to the increasing depth penetration. The geological boundaries of Fig. 1(a) are added for reference. At
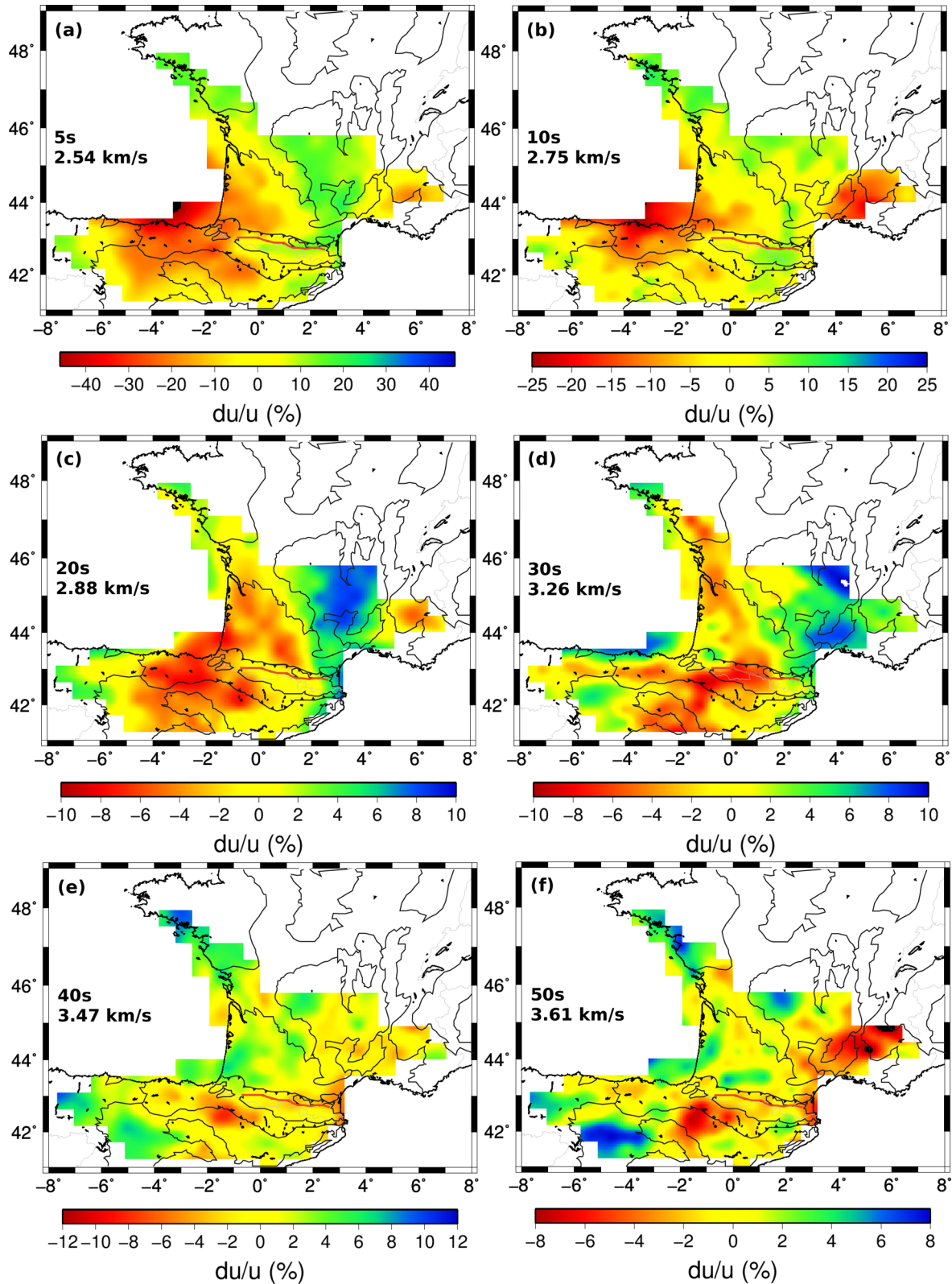
Figure 4. Maps of the group velocity relative variations at 5 s (a), 10 s (b), 20 s (c), 30 s (d), 40 s (e) and 50 s (f). The reference group velocity is given at the left-hand side of each panel. Grey lines, main geological boundaries; red line, North Pyrenean fault (see Fig. 1b). The group velocity relative variations are computed with respect to the mean group velocity at each frequency. Note horizontal smearing towards the south at the Cantabrian coast, as discussed in Section 5.1.3.

short periods ($T < 20$ s), there was very good agreement between the geological boundaries and the group velocity variations: the Ebro and Aquitaine sedimentary basins are characterized by low group velocities, whereas the axial zone of the Pyrenees is characterized by high group velocities. At longer periods ($T > 20$ s), the group velocities were mainly sensitive to the thickness of the crust, with, that is, low velocities in the areas of thick crust beneath the Pyrenees. To go further in the interpretation, the quality of the group velocity inversion needs to be analysed, and in particular the model resolution, before inverting the 3-D *Vs* model. This 3-D model is obtained by merging the information coming from the 1-D inversion of the dispersion curve at each gridpoint.

3.3.3 Resolution tests

The variance reduction (the reduction of the value of the penalty function between the input and the final models) is moderate, at between 80 per cent at short periods and 40 per cent at long periods (see Table 1). However, note that the input model already explains part of the raw data residuals, as we start with the model obtained after the final data rejection procedure. The overall data fit after the inversion is therefore good, as reflected in the average rms of the differences between the observed and predicted group velocities along each path (see Table 1, final rms).

The area of good resolution was defined based on the diagonal terms of the resolution matrix and the resolution length, as defined by Barmin *et al.* (2001). Fig. S3 shows these two parameters for three different periods. The well-resolved area was defined by cells where the diagonal terms of the resolution matrix was >0.3 and the resolution length was <150 km. An additional difficulty was encountered here, because these criteria are frequency dependent, while for the subsequent depth inversion there was the need to define the same resolved area across the whole period range. The period of 30 s was chosen, the approximate centre of our period interval, to define the area resolved in which the depth inversion was carried out.

Spike tests give additional information for resolution. Fig. 5 shows examples of such spike tests, for three different periods. The spike amplitudes are 25 per cent at 5 s, 10 per cent at 30 s and 8 per cent at 55 s. The synthetic data were calculated as simple

time delays, using the same paths as for the inversion of the field data. These time delays were transformed into velocities, and white noise of 0.1 km s^{-1} was added; that is, of the order of 3 per cent. As shown in Fig. 5, the geometry of the spikes was well recovered, while the recovered amplitude was dampened, as is common in seismic tomography procedures. The dampening in each point is model dependent, which is why it is not possible to correct for this effect in tomography models. As the size of the anomalies recovered were approximately the value of the smoothing parameters in the inversion, we conclude that our smoothing is relatively conservative, so that we could confidently proceed to the 3-D inversion where there was the need to combine the results from all of the periods.

4 DEPTH INVERSION

It remains a challenge to robustly invert group velocity dispersion curves for *Vs*(z) structures. For this reason, many studies have only produced group or phase velocity maps (e.g. Shapiro & Campillo 2004; Bensen *et al.* 2007; Seats *et al.* 2012; Verbeke *et al.* 2012). However, the depth inversion step is key to the imaging and interpretation of the 3-D structure, which was the main motivation of this study.

Whether based on noise correlations or earthquake data, the non-uniqueness of surface wave dispersion data inversion must be addressed. The simplest strategy is to consider smooth velocity profiles, so that the inversion converges to a solution even if the input model is not close to the 'real' Earth. Owing to the strong heterogeneity in the area, it was not possible to explain the observed dispersion curves with smooth models obtained using strong vertical damping and smoothing constraints. With relaxing of the regularization constraints, the inversions converged towards models with unrealistically strong vertical fluctuations in the velocity. Another strategy is to consider simple model parametrization, with a small number of parameters, which can be explored through nonlinear inversion, such as Monte Carlo approaches on which some statistical analysis can be applied (e.g. Brenguier *et al.* 2007; Stehly *et al.* 2009; Shen *et al.* 2013), or through Bayesian exploration of the model parameters, which are each associated with a probability function (e.g. Köhler *et al.* 2012). Although this strategy is less dependent on the starting model, this is closely associated with
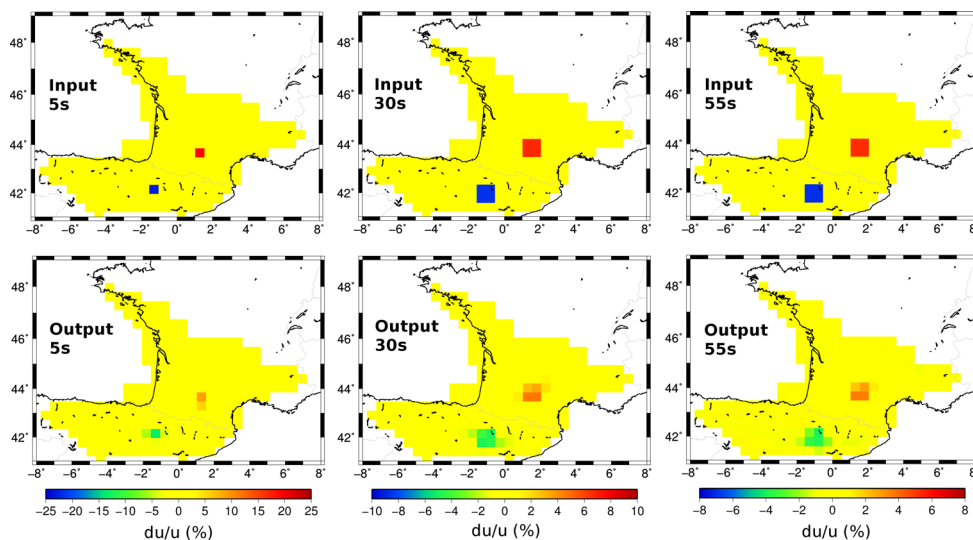
Figure 5. Spike tests of the inversion of the delay times for the group velocity at 5, 30 and 55 s. Top panel: input models. Bottom panel: results. The size of the anomalies is 40 km at 5 s, and 80 km at 30 s and 55 s.

the model parametrization, so it remains technically challenging to apply this to areas with very strong lateral variations of Earth structure for which an 'average' starting model of the area might be inadequate in most gridpoints. Many studies have in any case at least partly relied on inclusion of *a priori* information from other data analyses (e.g. Stehly *et al.* 2009; Li *et al.* 2012; Shen *et al.* 2013).

This data set is ideal to test the performance of a coherent and robust strategy for the inversion. First, the study area was particularly heterogeneous, and we wanted to be able to automatically accommodate for this heterogeneity in the inversion. Secondly, the station grid was almost regular, except for the Bay of Biscay. Finally, we had good Moho geometry estimates for comparison from receiver functions (Chevrot *et al.* 2014), and detailed knowledge of the basin thickness, as the area has been extensively studied, particularly for gas exploration purposes, among others. Below we suggest an automatic, robust and simple approach that should be useable for any type of study area, and which can be implemented with or without *a priori* knowledge from other types of analysis.

4.1 Method

Our suggested approach relied on the following steps:

• *Step* 1: Create a library of dispersion curves for a large set of earth models.
• *Step* 2: Select the 1000 models that best fit the observed dispersion curve.
• *Step* 3: Linearize the inversion using the average over 1000 models as the starting model.

As in Steps 1–2 we explore all of the combinations of the model parameters with a relatively rough parametrization, our approach combines elements of fully nonlinear inversion with the linearized inversion in Step 3.

Step 1: Model library

To build the library, the variety of models that can be expected across the study area were explored. To limit the dimension of the model space, a five-layer model was used, composed of a top low-velocity layer, a sedimentary layer, the crystalline part of the upper crust, the lower crust and the mantle. Each layer was defined by its thickness (except for the infinitely thick mantle), the seismic wave velocities, and the density. To define the range of velocities in each layer, sensible ranges of *Vp* were used, and these were translated into *Vs* (which dominates the inversion) using a *Vp/Vs* ratio of 1.73. The density, which is the second most influent parameter on the dispersion curve, was calculated using the Nafe–Drake relation:

$$\rho = 1.6612 \times Vp - 0.4712 - Vp^2 + 0.0671 \times Vp^3$$
$$- 0.0043 \times Vp^4 + 0.000106 \times Vp^5. \quad (2)$$

Table 2 shows the ranges in the *P*-wave velocity and layer thickness used to build the model library. The increment used for the layer thickness is 1 km for the two first layers (top and sedimentary layers) and 2 km for the layer of the crust. For the velocities, the increment is 0.5 km s^{-1}, except for the mantle for which the increment is 0.2 km s^{-1}.

A top layer was introduced to account for the possible presence of low velocities close to the surface in the basins. This shallow layer cannot be resolved in detail, as the minimum study period was 5 s, but it serves the purpose of accommodating such low

Table 2. Parameters used to build the library of Step 1 of the depth inversion.

Layer	Thickness range (km s^{-1})	*Vp* range (km)
Top layer	0–4	2–3
Sedimentary layer	0–12	3.0–5.5
Upper crust	10–26	5–6
Lower crust	10–26	6–7
Mantle	Infinite	7.5–8.1

surface velocities if they occur so as to avoid contamination below. Note that the vertical velocity variations within each layer will be obtained in inversion Step 3. Using the parameters of Table 2, a library of 2766555 models and their associated dispersion curves was obtained.

Step 2: Creating a starting model for the linearized inversion

At each gridpoint, the fits between the observed dispersion curve with those in the library were calculated, and the residuals over the whole period range were computed. The 1000 models with the lowest rms were then selected. As many models had very similar rms, the concept of the 'best' model was not relevant. A model that was representative of the 1000 'acceptable' models was thus determined (see further discussion of the choice of number of models at the end of this section). The main parameters were sufficiently stable to assume that in each gridpoint, we were close to a starting model that will not lead into a local minimum or into unrealistic models.

There were two options for the calculation of this model: either as the average of each parameter (nine in our case, as four for the depth, and five for the velocity in each layer); or as the average of the 1000 velocity models (we used 1-km depth intervals). In the first case, a 5-layer model was obtained, whereas a smoothed model was obtained for the second case. In the first case, the interfaces were easy to identify, so the interpretation of the models was straightforward. In our case, the 5-layer model was too simple to adequately explain the observed dispersion curves. Therefore, the second approach was used, which provided a significantly better data fit in Step 3. Interpretation of the final model (after Step 3) became more difficult, as the interfaces were not identified as such, but typically appeared as velocity gradients.

The best 1000 models, that is 0.03 per cent of the total number of models, typically have an rms smaller or equal to 1.5 times the best rms. If we set a lower limit for the allowed rms, the number of models used in the average quickly becomes very small, and tend to be dominated by single values of some velocities and/or interface depths. As our sampling of the parameter space is very rough, such limited classes of models with very strong interfaces are not ideal for the subsequent linearized inversion. Interestingly, and counter intuitively, the average of 1000 models generally has a better fit to the data than the average of a smaller number of better fitting models. Even though the choice of 1000 models is somewhat arbitrary, it provides a good compromise between individual model data fit, and smoothness of the resulting average model.

At the end of Step 2, in each gridpoint, we had a starting model that was used as input for the linearized inversion.

Step 3: Linearized inversion

The starting model at each grid node obtained after Step 2 was taken as the starting model for standard linearized inversion using the program package of Herrmann & Ammon (2002). As the Rayleigh

wave group dispersion curves were mostly sensitive to the *S*-wave velocities, this parameter was chosen for the inversion. The *P*-wave velocities and densities were derived from *Vs* with the same equations as those used for computing the library.

As we were working with a smooth model described with 1-km-thick layers, we inverted for *Vs* only. Convergence was typically achieved after four iterations. The smoothing constraints that could be applied were at this point sufficient to ensure that subsequent iterations, necessary for some points, did not induce additional oscillations in the model. To have a reference for rms improvement, we calculate the rms (0.063 km s^{-1}) using an average model across the whole study area. The average rms using the dispersion curve of the starting model in each gridpoint (after Step 2) was 0.046 km s^{-1}. The final average rms after Step 3 was 0.038 km s^{-1}; that is, significantly lower than the lateral variations in the group velocity, as for example, shown in Fig. 4. The final rms was spatially variable, as shown in Fig. S5, with an overall very low rms in the central part of the model, and an rms that remained everywhere smaller than the lateral variations in the group velocity.

5 CRUSTAL *Vs* MODEL: DISCUSSION

5.1 Quality assessment of the 3-D *Vs* model

Our velocity model is the first 3-D crustal model for the study area with uniform coverage and resolution. Prior to interpretation, and to assess the robustness of the data analysis and the inversion, we proceeded to comparisons with other geophysical studies in the area: deep seismic sounding profiles, and published maps of sediment thickness and crustal thickness. One difficulty in performing such comparisons is to map the depth of internal discontinuities from smooth 1-D *Vs* models. Two methods to extract the depth of interfaces were thus tested: by delineating these boundaries by picking an iso-velocity surface; or by selecting the extrema of the second derivative of *Vs*(z) to pick the strongest changes in the velocity gradient. Both of these methods led to similar fits to the published data on average. In the following, we show the comparisons using iso-velocity surfaces for both the basement depth (2.9 km s^{-1}; see Section 5.1.2) and the Moho depth (4 km s^{-1}; see Section 5.1.3).

5.1.1 Comparison with ECORS deep seismic sounding profiles

Fig. 6 shows our 3-D *Vs* model along vertical sections following the two ECORS deep seismic sounding profiles of the central Pyrenees (Choukroune *et al.* 1989; Fig. 6a) and western Pyrenees–Arzacq (Daignières *et al.* 1994; Fig. 6b). The white lines in Fig. 6(a) represent the reflectors in the ECORS profiles after migration, while in Fig. 6(b), they show the interpretation of the main ECORS reflectors made by Choukroune *et al.* (1989). The black lines are the 2.9 and 4.0 km s^{-1} iso-velocity curves in our *Vs* model. The lateral variations in *Vs* show striking agreement with the positions of the major deep seismic sounding reflectors. The general shape of the Moho is well retrieved by our ambient noise tomography, including the strong depth change between the thick Iberian crust to the south and the thinner European crust to the north. We also find a low velocity anomaly (3.8 km s^{-1}) in the deep crust beneath the Axial Zone of the Pyrenees (Fig. 6a), which could be related to the underthrust of the Iberian crust beneath the European crust, as proposed in the interpretation of the ECORS profile. The thin-skinned duplexes of the Arize Massif in the central Pyrenees (Fig. 6a; Roure *et al.* 1989) have a clear low-*Vs* signature in the upper crust (<3.3 km s^{-1})
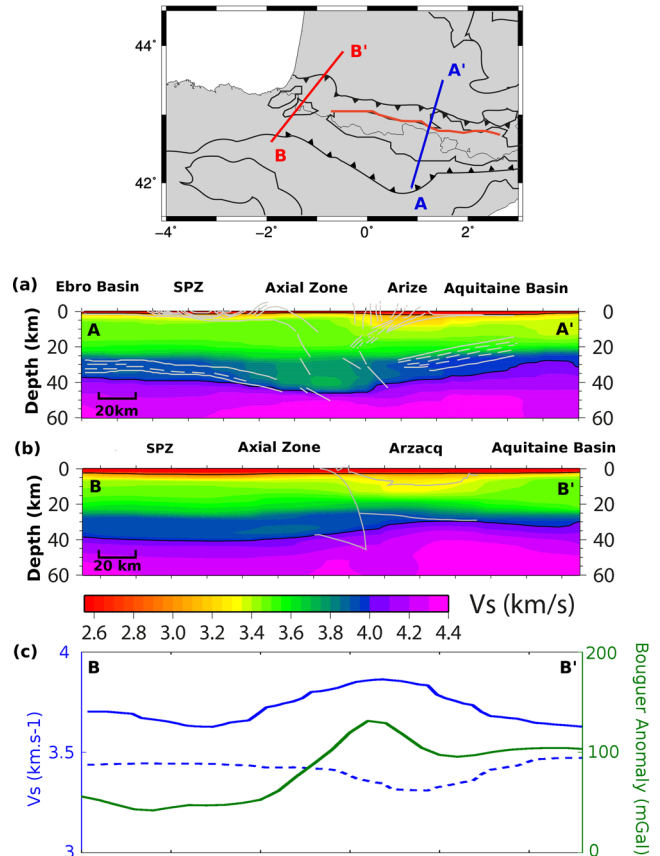

Figure 6. Comparison of the ECORS deep seismic sounding profile of the central Pyrenees (a; A–A′) and western Pyrenees–Arzacq (b; B–B′), with the corresponding depth sections in our 3-D *Vs* model. Top panel: map showing the locations of the profiles. Black solid lines in (a) and (b), iso-velocities of 2.9 and 4 km s^{-1}, which correspond to the top of the basement and the Moho, respectively. (c) *S*-wave velocity at 10 km in depth (dashed blue line), at 25 km in depth (solid blue line), and the Bouguer anomaly (green line) along the western Pyrenees–Arzacq profile.

beneath the North Pyrenean Zone. This along-strike velocity contrast in the upper 10 km demonstrates the structural differences between the North Pyrenean Zone and the South Pyrenean Zone. In the second profile, the deep Arzacq basin is also clearly seen in the velocity model (Fig. 6b).

5.1.2 Thickness of the sedimentary layer

The iso-velocity surface *Vs* = 2.9 km s^{-1} was used to map the basement depth in Fig. 7(a). Recovering this interface with the ambient noise correlation method is a challenge in areas such as ours, where there are strong changes in sediment thickness. The comparison of Fig. 7(a) with the map compiled by Theunissen *et al.* (2013), which is shown in Fig. S6, is however satisfactory, as we correctly retrieve the geometry of the main sedimentary basins, while we underestimate the maximum thickness of the Ebro and Aquitaine basins, as their deepest parts are narrower than our grid node spacing (40 km). The maximum thickness of the southeastern basin is better estimated due to its wider extent. Conversely, we overestimate the thickness of the Basque–Cantabrian basin, which is 5 km and not 8 km as in Fig. 7(a). These large thickness values are explained by the very weak velocities observed at 3 km to 5 km in depth in this area (see map views of Figs 8a and b). This
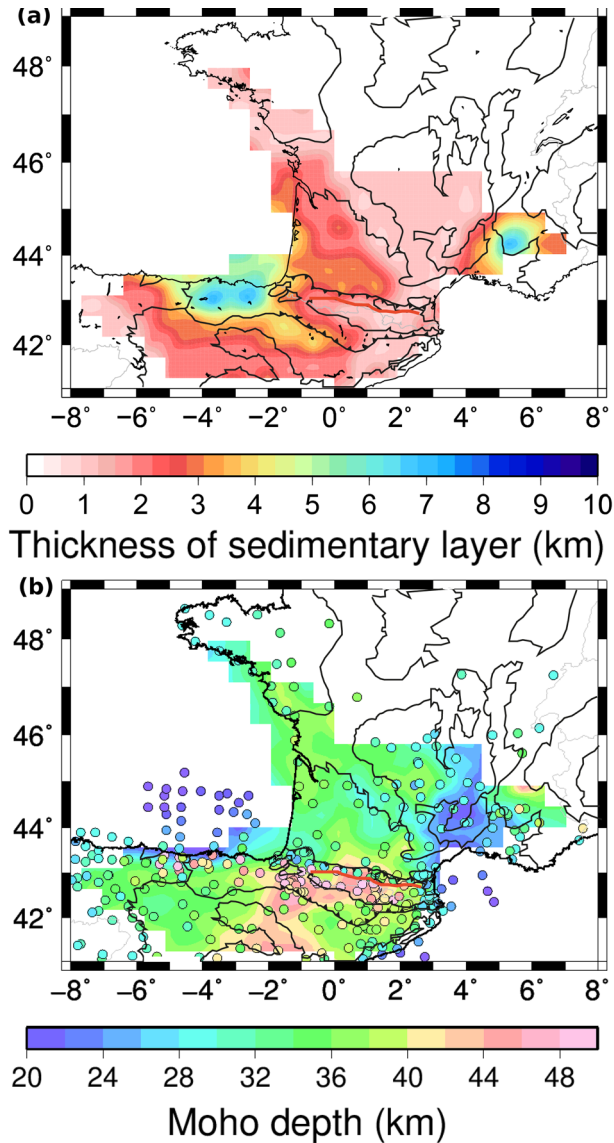
Figure 7. Maps of the iso-velocity depths: (a) Iso-velocity $Vs = 2.9$ km s^{-1} associated with the top of the basement. (b) Iso-velocity $Vs = 4$ km s^{-1} associated with the crust–mantle boundary. Filled circles, Moho depth values that Chevrot *et al.* (2014) estimated from receiver functions or compiled from seismic reflection–refraction studies; solid black lines, main geological boundaries of Fig. 1(b). The discrepancy in Moho depth observed along the Cantabrian coast is discussed in Section 5.1.3

might be related to the proximity of the passive margin of the Bay of Biscay and the thick water layer. Picking an iso-velocity surface as the basement depth is not appropriate in this area.

5.1.3 Moho depth

To estimate the Moho depth, we searched for the velocity value that minimized the rms difference between the crustal thickness estimates by the receiver functions of Chevrot *et al.* (2014) and the iso-velocity surfaces in our 3-D model. The best fit was obtained with iso-velocity $Vs = 4$ km s^{-1}, for which the agreement with the ECORS deep seismic sounding profiles is also excellent (see Section 5.1.1). Fig. 7(b) shows our Moho depth estimate, as well as those of Chevrot *et al.* (2014), as filled circles using the same colour scale. Our Moho map retrieves all of the major features of the

Moho structure, which is dominated by the difference in the crustal thickness between the thick crust beneath the Pyrenees and the thin crust beneath the southern margin of the Bay of Biscay, the southeastern basin, and the southeastern part of the Massif Central. The differences that we observe in the southeastern part of the Massif Central are well explained by the results from an early refraction profile of Perrier & Ruegg (1973), who identified an unusual crustal structure in that area, with a shallow velocity discontinuity from 6 to 7.3 km s^{-1}, at 24 km in depth beneath the Oligocene basins and the volcanoes of the Massif Central (close to our 22 km estimate) and an absence of a clearly defined Moho. We further discuss this anomalous structure in Section 5.2.3. A small area south-east of the Massif Central, in the south-eastern basin, has a non-explained difference in Moho thickness of 3–5 km (we observe 22 km thickness while Chevrot *et al.* (2014) observed 25–27 km thickness). Another area with a misfit was at the southern edge of the study zone, but well resolved according to our resolution analysis, between –4° and 0° longitude (Iberian chain, Almazan basin and western part of the Ebro basin) where we observed a Moho that was 6 km deeper than that inferred by Chevrot *et al.* (2014). This difference is not linked to the inversion procedure, as it corresponds to relatively low group velocities at long periods (Fig. 4), which translate into a thicker crust. Finally, the differences in the Moho depths observed beneath the Cantabrian Mountains and the Basque–Cantabrian basin (28– 29 km, instead of 40–44 km in Chevrot *et al.* 2014) are related to anomalous short-period dispersion curves. The difference can be explained by a particular combination of strong lateral structural variations in a location at the edge of the seismic network which is not reflected in the resolution matrix. The crust of the Cantabrian Mountains is thick (50 km) as compared to the thin (about 25 km) oceanic crust of the Bay of Biscay, which includes a thick sedimentary layer. We identify the north-south change in crustal thickness, but it is shifted 60-km southward, that is approximately one interstation distance. Shapiro *et al.* (1998) showed that at the edge of a continent, part of the energy between two points on the coast is channelled through the slow oceanic structures. Our group velocities between stations along the coast have indeed in many cases anomalously slow velocities. Additionally, resolution tests show that even though spikes are resolved, a strong negative velocity anomaly in the Bay of Biscay spreads to the south even in the presence of a neighbouring high E–W velocity anomaly along the coast.

5.2 Highlights of the 3-D *Vs* model

The exploration of the 3-D *Vs* model is likely to continue to yield new insights into the dynamics of all or parts of these studies for several years, in combination with other geophysical and geological studies. In this section we first present the 3-D *Vs* model in the form of depth slices, which contain complementary information to that presented in the maps of the interface depths. We then focus on two results that are associated with the much-discussed issue of explaining the Bouguer anomaly in the Labourd–Mauléon–Arzacq region and with a large-scale anomaly of the lithospheric structure beneath part of the Massif Central.

5.2.1 Depth slices and brief description of the 3-D Vs model

Fig. 8 shows six horizontal slices at 3–35 km in depth in our 3-D *Vs* model. At depths of 3 km (Fig. 8a) and 5 km (Fig. 8b), the *Vs* maps are consistent with the surface geology. The sedimentary basins (Basque–Cantabrian, Aquitaine, Ebro basins, and part of the
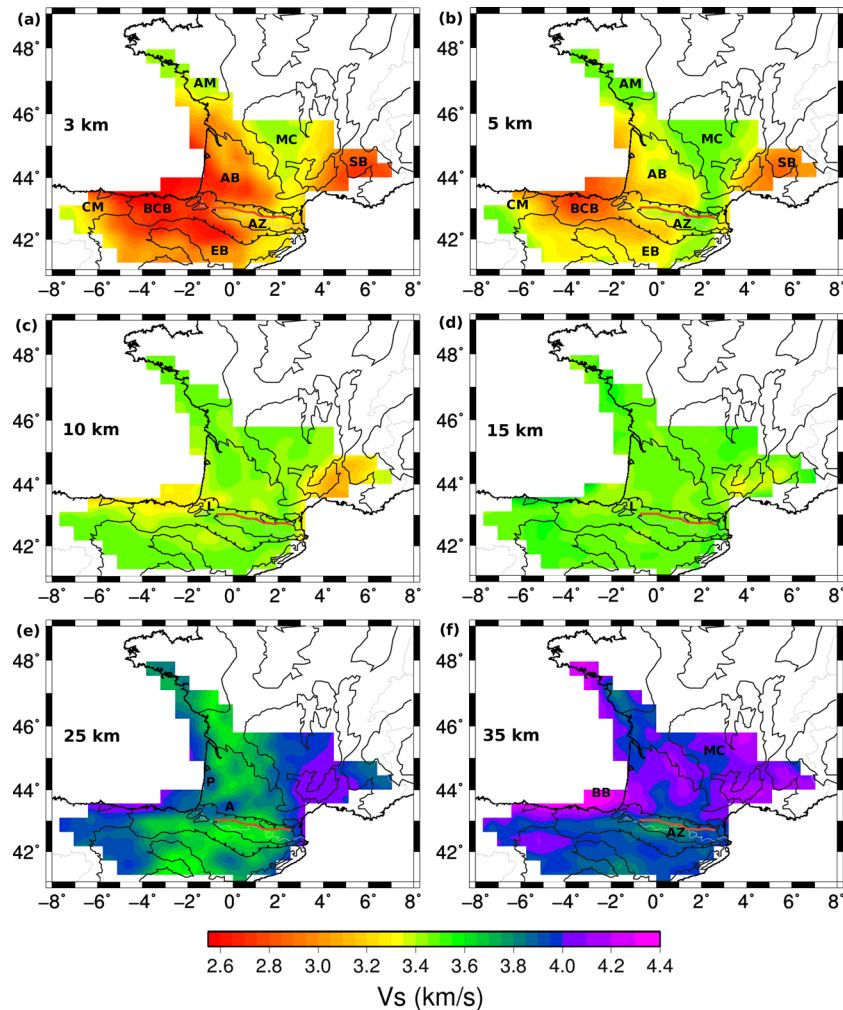
Figure 8. Depth slices at 3 km (a), 5 km (b), 10 km (c), 15 km (d), 25 km (e) and 35 km (f) in depth. Solid black lines, main geological boundaries of Fig. 1(b). A, Labourd–Mauléon–Arzacq velocity anomaly; AB, Aquitaine basin; AM, Armorican Massif; AZ, Axial Zone of the Pyrenees; BB, Bay of Biscay; BCB, Basque–Cantabrian basin; CM, Cantabrian mountains; EB, Ebro basin; L, Labourd–Mauléon area; MC, Massif Central; P, Parentis velocity anomaly; SB, southeastern basin.

southeastern basin) have low *S*-wave velocities (2.6–3.4 km s^{-1}), whereas the outcrops of the Variscan basement (Axial Zone of the Pyrenees, Massif Central and Armorican Massif) have high velocities (up to 3.6 km s^{-1}). The only exception is the basement outcrop of the Cantabrian Mountains, which has lower *S*-wave velocities than the other massifs, of 3.2 km s^{-1} at 5 km in depth. Although the Axial Zone of the Pyrenees is made of crystalline basement, its velocities at 3 km in depth are slightly lower than those of the Massif Central and Armorican Massif (3.15 and 3.35 km s^{-1}, respectively). This difference disappears at 5 km in depth. The velocities are more laterally homogeneous at 10 and 15 km in depth than at shallow depths (Figs 8c and d). At 35 km in depth (Fig. 8f), this is close to the crust–mantle boundary, except beneath the Pyrenees. The velocities are >4 km s^{-1} beneath the Massif Central and the Bay of Biscay, which have thin crusts. The velocities are lower (3.75 km s^{-1}) under the Axial Zone of the Pyrenees, where the crust is thick.

5.2.2 Focus area 1: the Labourd–Mauléon–Arzacq region (western Pyrenees)

In the northwestern part of the Pyrenees, beneath the Labourd–Mauléon area, Vacher & Souriau (2001) and Jammes *et al.*

(2010) proposed that the 140-mGal positive Bouguer anomaly is generated by a high-density body located between the near-surface and 12 or 16 km in depth. The size of this high-velocity body is smaller than our resolution, so we cannot rule out its presence. It is, however, striking that our model is characterized by low *Vs* at 10 and 15 km in depth (Figs 8c and d) in the Labourd–Mauléon area, as compared to the neighbouring areas. More significantly, at 25 km in depth (Fig. 8e), the larger-sized Labourd–Mauléon–Arzacq region is characterized by high *S*-wave velocities of up to 3.95 km s^{-1}. These high *Vs* at 25 km in depth along the western Pyrenees–Arzacq ECORS profile are compared to the Bouguer anomaly with lateral variations of *Vs* at 10 and 25 km in depth in Fig. 6(c). The Labourd gravity anomaly is spatially correlated with the *Vs* profile at 25 km in depth, and anticorrelated with the *Vs* profile at 10 km in depth. Fig. 8(e) shows a similar high-velocity anomaly at 25 km in depth in the Parentis region, in the direct on-land continuation of the offshore Parentis basin. We therefore suggest that the two lower crustal high-velocity anomalies of the Parentis and Labourd–Mauléon–Arzacq regions are traces of the two ancient hyper-extended Bay of Biscay–Parentis and Pyrenean–Basque–Cantabrian rift systems, as proposed by Tugend *et al.* (2014).
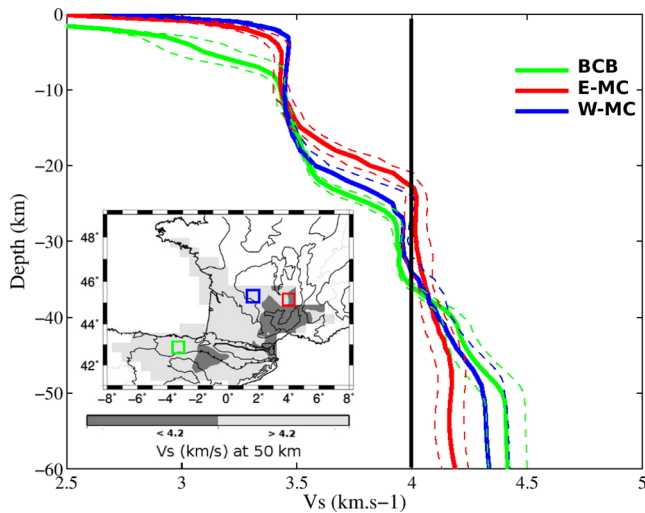
Figure 9. Average *S*-wave velocity–depth models for the Basque–Cantabrian Basin (BCB; solid green curve), the western part of the Massif Central (W-MC; solid red curve), and the eastern part of the Massif Central (E-MC; solid blue curve). The average models are calculated over four neighbouring grid nodes. The $\bar{V}s \pm 1\sigma$ curves are shown as dashed lines. Black solid line, iso-velocity 4 km s^{-1} that we associate with the Moho. Inset: map showing *Vs* at 50 km in depth, and the location of the BCB, W-MC and E-MC zones (open squares).

5.2.3 Focus area 2: the Massif Central

Fig. 9 shows three velocity–depth models for two areas in the Massif Central (Fig. 9, red, blue) and one in the Basque–Cantabrian basin (Fig. 9, green). The Basque–Cantabrian basin model is shown as an example of the typical *Vs(z)* profiles in the basin areas of the study region, with low velocities at shallow depths, a crystalline upper crust with almost constant velocity, a strong gradient to a constant and high-velocity lower crust, and a strong velocity gradient at the crust–mantle boundary. At depths of >8 km, the western Massif Central model (Fig. 9, blue) is similar to the reference model of the Basque–Cantabrian basin. The eastern Massif Central model (Fig. 9, red) has different characteristics, with a strong velocity gradient between 15 and 22 km in depth that results in a shallow crossing of the 4 km s^{-1} iso-velocity considered as the Moho depth, and very slowly increasing velocities at depths >22 km. The *P*-wave velocity model estimated by Perrier & Ruegg (1973) from refraction studies in the same area has similar characteristics, with a sharp velocity increase from 6 to 7.3 km s^{-1} at 24 km in depth, followed by a velocity gradient. The main difference is the strength of the velocity gradient as *Vs* at 45 km in depth is only 4.2 km s^{-1}, while *Vp* in the refraction model is 8.4 km s^{-1} (Fig. 9). Perrier & Ruegg (1973) interpreted the discontinuity at 24 km in depth as the transition from the crust to an anomalous upper mantle, while we interpret the sharp discontinuity at 22 km in depth as the Moho.

Fig. 9 shows that the velocity below 50 km in depth is lower in the eastern Massif Central (4.2 km s^{-1}) than in the two other regions (4.3 and 4.4 km s^{-1}). The map in the inset in Fig. 9 shows the areas with *Vs* < 4.2 km s^{-1} at 50 km in depth, which are located in the southeastern Massif Central and at the western end of the Ebro basin. Although our *Vs* values should be considered with caution at depths >40 km, we note that the low *Vs* anomaly beneath the southeastern Massif Central coincides with the low *P*-wave velocity anomaly imaged at the upper-mantle depth by the teleseismic traveltime tomography of Chevrot *et al.* (2014).

6 CONCLUSIONS

Using records of a dense seismic array with 60-km average inter-station spacing, we have computed the first high-resolution 3-D *Vs* model of the crust of the Pyrenees and the surrounding areas of southwestern France and northern Spain. The main challenge of the study was to obtain a robust model despite the strong lateral variability of the crustal structure. Our proposed inversion scheme meets these requirements, through the combination of elements from full nonlinear inversion through systematic exploration of the model space, and from classical linearized inversion using vertically smoothed models. The comparison shows good agreement with the known geological structures, in spite of the localized differences, for which we offer explanations in most cases.

Our model sheds light on the long-lasting discussion concerning the crustal structure in the Labourd–Mauléon area in the western part of the North Pyrenean Zone, which shows the strongest gravity anomaly of the Pyrenees. Our data show that the origin of the anomaly is most likely located in the lower crust, where we identify a high-velocity body beneath the gravity anomaly. As we find a similar high *Vs* anomaly at 25 km in depth beneath the Parentis region, we suggest that these two lower crustal velocity anomalies of the Labourd–Mauleon and Parentis areas might be imprints of the Albian–Aptian rifting phase of extreme crustal thinning and mantle denudation (Jammes *et al.* 2010; Lagabrielle *et al.* 2010; Tugend *et al.* 2014). A rather unexpected new result is associated with the southeastern part of the Massif Central, where the *Vs* profiles are very similar to the *Vp* profiles proposed for the Oligocene basins by Perrier & Ruegg (1973) based on refraction profiling. Our data suggest that rather than being an anomaly of intracrustal velocities, the anomaly is that of crustal thinning (to a thickness of 21–25 km) and low upper-mantle velocities, which cover a relatively large area within the Massif Central. These highlights provide a foretaste of the potential outcomes of this first high-resolution 3-D crustal *Vs* model for reconstruction of the evolutionary models of the Pyrenees and adjoining areas, in combination with geological and other geophysical studies.

REFERENCES

Baig, A.M., Campillo, M. & Brenguier, F., 2009. Denoising seismic noise correlations, *J. geophys. Res.,* **114,** B08310, doi:10.1029/2008JB006085.

Barmin, M.P., Ritzwoller, M.H. & Levshin, A.L., 2001. A fast and reliable method for surface wave tomography, *Pure appl. Geophys.,* **158,** 1351–1375.

Bensen, G.D., Ritzwoller, M.H., Barmin, M.P., Levshin, A.L., Lin, F., Moschetti, M.P., Shapiro, N.M. & Yang, Y., 2007. A fast and reliable method for surface wave tomography, *Geophys. J. Int.,* **169,** 1239–1260.

Boué, P., Poli, P., Campillo, M., Pedersen, H., Briand, X. & Roux, P., 2013. Teleseismic correlations of ambient seismic noise for deep global imaging of the Earth, *Geophys. J. Int.,* **194,** 844–848.

Brenguier, F., Shapiro, N.M., Campillo, M., Nercessian, A. & Ferrazzini, V., 2007. 3-D surface wave tomography of the Piton de la Fournaise volcano using seismic noise correlations, *Geophys. Res. Lett.,* **34,** L02305, doi:10.1029/2006GL028586.

Briand, X., Campillo, M., Brenguier, F., Boué, P., Poli, P., Roux, P. & Takeda, T., 2013. Processing of terabytes of data for seismic noise analysis with the Python codes of the Whisper Suite, in *Proceedings of the AGU Fall Meeting*, Abstract n°IN51B-1544, San Francisco, CA, 9–13 December.

Campillo, M. & Paul, A., 2003. Long-range correlations in the diffuse seismic coda, *Science,* **299,** 547–549.

Chazalon, A., Campillo, M., Gibson, R. & Carreno, E., 1993. Crustal wave propagation anomaly across the Pyrenean Range. Comparison between observations and numerical simulations, *Geophys. J. Int.,* **115,** 829–838.

Chevrot, S., Sylvander, M., Benahmed, S., Ponsolles, C., Lefèvre, J.M. & Paradis, D., 2007. Source locations of secondary microseisms in western Europe: evidence for both coastal and pelagic sources, *J. geophys. Res.,* **112,** B11301, doi:10.1029/2007JB005059.

Chevrot, S., Villaseñor, A. & Sylvander, M., 2014. High resolution imaging of the Pyrenees and Massif Central from the data of the PYROPE and IBERARRAY portable array deployments, *J. geophys. Res*, in press.

Choukroune, P. & Mattauer, M., 1978. Tectonique des plaques et Pyrénées: sur le fonctionnement de la faille transformante nord-pyrénéenne; Comparaison avec des modèles actuels, *Bull. Soc. Géol. France,* **7,** 689–700.

Choukroune, P. & ECORS Team, 1989. The ECORS Pyrenean deep seismic profile reflection data and overall structure of an orogenic belt, *Tectonics,* **8**(1), 23–39.

Choukroune, P., 1992. Tectonic evolution of the Pyrenees. *Annu. Rev. Earth planet. Sci.,* **20,** 143–158.

Cupillard, P., Stehly, L. & Romanowicz, B., 2011. The one-bit noise correlation: a theory based on the concepts of coherent and incoherent noise, *Geophys. J. Int.,* **184,** 1397–1414.

Daignières, M., Séguret, M. & Specht, M. ECORS team, 1994. The Arzacq-Western Pyrenees ECORS deep seismic profile, *Hydrocarbon Petrol. Geol. France: Spec. Publ. Eur. Assoc. Petrol. Geosci.,* **4,** 199–208.

Díaz, J., Villaseñor, A., Gallart, J., Morales, J., Pazos, A., Córdoba, D., Pulgar, J. & García-Lobón, J.L. *et al.*, 2009. *Orfeus Newslett.,* **8,** 2.

ECORS Pyrenees Team, 1988. The ECORS deep reflection seismic survey across the Pyrenees, *Nature,* **331,** 508–511.

Froment, B., Campillo, M., Roux, P., Gouédard, P., Verdel, A. & Weaver, R.L., 2010. Estimation of the effect of nonisotropically distributed energy on the apparent arrival time in correlations, *Geophysics,* **75**(5), SA85–SA93.

Groos, J-C., Bussat, S. & Ritter, J.R.R, 2012. Performance of the different processing schemes in seismic noise cross-correlation, *Geophys. J. Int.,* **188,** 498–512.

Herrmann, R.B. & Ammon, C.J, 2002. Computer programs in seismology version 3.20: Surface waves, receiver functions and crustal structure, Saint Louis University, Available at: http://www.eas.slu.edu/People/RBHerrmann/CPS330.html, 110 pp.

Hillers, G., Graham, N., Campillo, M., Kedar, S., Landès, M. & Shapiro, N.M, 2012. Global oceanic microseism sources as seen by seismic arrays and predicted by wave action models, *Geochem. Geophys. Geosyst.,* **13**(1), Q01021, doi:10.1029/2011GC003875.

Jammes, S., Manatschal, G., Lavier, L. & Masini, E., 2009. Tectonosedimentary evolution related to extreme crustal thinning ahead of a propagating ocean: example of the western Pyrenees, *Tectonics,* **28,** TC4012, doi:10.1029/2008TC002406.

Jammes, S., Tiberi, C. & Manatschal, G., 2010. 3D architecture of a complex transcurrent rift system: the example of the Bay of Biscay-Western Pyrenees, *Tectonophysics,* **489,** 210–226.

Kedar, S., Longuet-Higgins, M., Webb, F., Graham, N., Clayton, R. & Jones, C., 2007. The origin of deep ocean microseisms in the North Atlantic Ocean. *Proc. R. Soc.,* **464**(2091), 777–793.

Köhler, A., Weidle, C. & Maupin, V., 2012. Crustal and uppermost mantle structure of southern Norway: results from surface wave analysis of ambient noise and earthquake data, *Geophys. J. Int.,* **191,** 1441–1456.

Lagabrielle, Y. & Bodinier, J.L., 2008. Submarine reworking of exhumed subcontinental mantle rocks: field evidence from the Lherz peridotites, French Pyrenees, *Terra Nova,* **20,** 11–21.

Lagabrielle, Y., Labaume, P. & de Saint Blanquat, M., 2010. Mantle exhumation, crustal denudation, and gravity tectonics during Cretaceous rifting in the Pyrenean realm (SW Europe): insights from the geological setting of the lherzolite bodies, *Tectonics,* **29,** TC4012, doi:10.1029/2009TC002588.

Le Pichon, X., Bonnin, J. & Sibuet, J.C., 1970. La faille nord-pyrénéenne: Faille transformante liée à l'ouverture du golfe de Gascogne, *Comptes Rendus de l'Académie des Sci.,* **271,** 1941–1944.

Levshin, A.L., Yanocskaya, T.B., Lander, A.V., Bukchin, B.G., Barmin, M.P., Ratnikova, L.I. & Its, E.N., 1989. *Seismic Surface Waves in a Laterally Inhomogeneous EARTH,* Kluwer Academic Publishers.

Li, H., Li, S., Song, X.D., Gong, M., Li, X. & Jia, J., 2012. Crustal and uppermost mantle velocity structure beneath northwestern China from seismic ambient noise tomography, *Geophys. J. Int.,* **188,** 131–143.

Mordret, A., Landès, M., Shapiro, N.M., Singh, S.C., Roux, P. & Barkved, O.I, 2013. Near-surface study at the Valhall oil field from ambient noise surface wave tomography, *Geophys. J. Int.,* **193**(3), 1627–1643.

Pedersen, H.A.T., Krüger, F. & the SVEKALAPKO Seismic Tomography Working Group, 2007. Influence of the seismic noise characteristics on noise correlations in the Baltic Shield, *Geophys. J. Int.,* **168,** 197–210.

Perrier, G. & Ruegg, J.C., 1973. Structure profonde du Massif Central français, *Ann. Géophys.,* **29**(4), 435–502.

Poli, P., Pedersen, H.A., Campillo, M. & the POLENET/LAPNET Working Group, 2012a. Emergence of body waves from cross-correlation of a short period seismic noise, *Geophys. J. Int.,* **188,** 549–558.

Poli, P., Campillo, M., Pedersen, H.A. & the POLENET/LAPNET Working Group, 2012b. Body-wave imaging of Earth's mantle discontinuities from ambient seismic noise, *Science,* **338**(6110), 1063–1065.

Poli, P., Pedersen, H.A., Campillo, M. & the POLENET/LAPNET Working Group, 2013. Noise directivity and group velocity tomography in a region with small velocity contrast: the northern Baltic shield, *Geophys. J. Int.,* **192,** 413–424.

Roure, F. *et al.*, 1989. ECORS deep seismic data and balanced croos sections: geometric constraints on the evolution of the Pyrenees. *Tectonics,* **8**(1), 41–50.

Schimmel, M., Stutzmann, E. & Gallart, J., 2011. Using instantaneous coherence for signal extraction from ambient noise data at a local to a global scale, *Geophys. J. Int.,* **184,** 494–506.

Seats, K.J., Lawrence, J.F. & Prieto, G.A., 2012. Improved ambient noise correlation functions using Welch's method, *Geophys. J. Int.,* **188,** 513–523.

Sens-Schönfelder, C., Margerin, L. & Campillo, M., 2009. Laterally heterogeneous scattering explain Lg blockage in the Pyrenees, *J. geophys. Res.,* **114,** B07309, doi:10.1029/2008JB006107.

Shapiro, N.M., Campillo, M., Singh, S.K. & Pacheco, J., 1998. Seismic channel waves in the accretionary prism of the Middle America Trench, *Geophys. Res. Lett.,* **25.1,** 101–104.

Shapiro, N.M. & Campillo, M., 2004. Emergence of broadband Rayleigh waves from correlations of the ambient seismic noise, *Geophys. Res. Lett.,* **31,** L07614, doi:10.1029/2004GL019491.

Shapiro, N.M., Campillo, M., Stehly, L. & Ritzwoller, M.H., 2005. High-resolution surface-wave tomography from ambient seismic noise, *Science,* **307,** 1615–1618.

Shen, W., Ritzwoller, M.H. & Schulte-Pelkum, V., 2013. A 3-D model of the crust and the uppermost mantle beneath the Central and Western US by joint inversion of receiver functions and surface wave dispersion, *J. geophys. Res.,* **118,** 262–276.

Sibuet, J.C., Srivastava, S.P. & Spakman, W., 2004. Pyrenean orogeny and plate kinematics, *J. geophys. Res.,* **109,** B08104, doi:10.1029/2003JB002514.

Souriau, A. & Granet, M., 1995. A tomographic study of the lithosphere beneath the Pyrenees from local and teleseismi data, *J. geophys. Res.,* **100**(B9), 18 117–18 134.

Souriau, A., Chevrot, S. & Olivera, C., 2008. A new tomographic image of the Pyrenean lithosphere from teleseismic data, *Tectonophysics,* **460,** 206–214.

Stehly, L. & Cupillard, P., 2014. Modulating the distribution of noise sources that contribute to seismic-noise correlations, *Geophys. J. Int*, in press.

Stehly, L., Campillo, M. & Shapiro, N.M., 2006. A study of the seismic noise from its long-range correlation properties, *J. geophys. Res.,* **111,** B10306, doi:10.1029/2005JB004237.

Stehly, L., Fry, B., Campillo, M., Shapiro, N.M., Guilbert, J., Boschi, L. & Giardini, D., 2009. Tomography of the Alpine region from observations of seismic ambient noise, *Geophys. J. Int.,* **178,** 338–350.

Theunissen, T., Chevrot, S., Sylvander, M., Monteiller, V., Villaseñor, A., Benahmed, S. & Calvet, M., 2013. 3D crustal and lithospheric structure of the Pyrenean orogenic wedge, in *Proceedings of the EGU General Assembly, Abstract n° 2013–4000,* Vienna, Austria, 7–12 April.

Tugend, J., Manatschal, G., Kusnir, N.J, Masini, E., Mohn, G. & Thinon, I., 2014. Formation and deformation of hyperextended rift systems: insights from rift domain mapping in the Bay of Biscay-Pyrenees, *Tectonics,* **33,** doi:10.1002/2014TC003529.

Vacher, P. & Souriau, A., 2001. A three-dimensional model of the Pyrenean deep structure based on gravity modelling, seismic images and petrological constraints, *Geophys. J. Int.,* **145,** 460–470.

Verbeke, J., Boschi, L., Stehly, L., Kissling, E. & Michelini, A., 2012. High-resolution Rayleigh-wave velocity maps of central Europe from a dense ambient-noise data set, *Geophys. J. Int.,* **188,** 1173–1187.

Vissers, R.L.M. & Meijer, P.Th., 2012. Mesozoic rotation of Iberia: subduction in the Pyrenees?, *Earth-Sci. Rev.,* **110,** 93–110.

SUPPORTING INFORMATION

Additional Supporting Information may be found in the online version of this article:

Figure S1. Group velocity dispersion curves for three stations pairs, corresponding to three areas (Pyrenees range in blue, Aquitaine basin in red, Bay of Biscay in green). Inset: Map showing the locations of the station pairs.

Figure S2. L-curves at 5 s period. The damping varies between 40 and 750 (solid lines) and the lateral smoothing varies between 50 and 1500 km (symbols). The black large dot is the selected couple of parameters, damping = 100, lateral smoothing = 200 km.

Figure S3. Maps of the path density (top), resolution length (middle), and diagonal of the matrix of resolution (bottom) at 5, 30 and 55 s. Red filled triangles (top panels), station locations.

Figure S4. Maps of the group velocity relative variations at 15 s before (a) and after (b) interpolation. The average group velocity used for computing du/u was 2.73 km s^{-1}.

Figure S5. The rms between the observed and calculated dispersion curves after the linearized inversion.

Figure S6. Map of the sediment thickness compiled by Theunissen *et al.* (2013) (http://gji.oxfordjournals.org/lookup/suppl/doi:10.1093/gji/ggu270/-/DC1).

Please note: Oxford University Press is not responsible for the content or functionality of any supporting materials supplied by the authors. Any queries (other than missing material) should be directed to the corresponding author for the article.